Cyclic depopulation of edge states in a large quantum dot

New Journal of Physics

Cyclic depopulation of edge states in a large quantum dot

S Baer[1]**, C Rössler, T Ihn, K Ensslin, C Reichl and W Wegscheider**

Solid State Physics Laboratory, ETH Zurich, 8093 Zurich, Switzerland
E-mail: sbaer@phys.ethz.ch

Abstract. We investigate the magneto-transport through a $1.6\,\mu$m wide quantum dot (QD) with an adjacent charge detector, for different integer filling factors in the QD and constrictions. When this system is operated at a high transmission, it acts as a Fabry–Pérot interferometer, where transport is governed by a Coulomb blockade mechanism. For lower transmissions where the barriers are in the tunneling regime, we can directly measure the charge stability diagram of two capacitively and tunnel-coupled Landau levels. The tunneling regime has been investigated in direct transport, as well as in single-electron counting. The edge states within the dot are non-cyclically depopulated, which can be explained by a simple capacitive model and allows to draw conclusions about the edge state geometry within the QD.

---

[1] Author to whom any correspondence should be addressed.

IOP Institute of Physics **Φ** DEUTSCHE PHYSIKALISCHE GESELLSCHAFT

Contents

1. Introduction

Two-dimensional electron systems at low temperatures and in strong magnetic fields show a rich spectrum of highly degenerate, incompressible ground states [1, 2]. Fractional quantum Hall states, occurring at a fractional filling factor ν with an odd denominator, are well described by the Laughlin wavefunction [3]. There exists a prominent exception from this hierarchy: the $\nu = \frac{5}{2}$ state [4], which is believed to obey non-abelian statistics [5, 6]. This remarkable property could make it an interesting candidate for the realization of a topological qubit [7]. Theoretical ideas on probing the statistics of the $\nu = \frac{5}{2}$ state rely on the use of quantum dots (QDs), which are operated as Fabry–Pérot interferometers [8–12].

QDs exposed to a magnetic field also offer other interesting fields of study, such as the investigation of the spin configuration [13] or few-electron addition spectra [14]. In the presence of a strong magnetic field, Coulomb blockade (CB) oscillations can no longer be described within a single-particle picture. Alternating compressible and incompressible regions are formed inside the dot, which can strongly modify the CB oscillations [15]. Previous experiments have allowed the extraction of mutual capacitances of these regions for different filling factors [16]. In those experiments, alternating high and low CB peak currents have been observed, which was attributed to a double dot-like behavior of two edge states inside the dot. However, for the interpretation of recent experiments using QDs as Fabry–Pérot interferometers [17–19], it is important to understand the detailed structure of edge states inside the QD and the parameter range where this description is valid.

Here, we present investigations on a large QD with a quantum point contact (QPC) serving as a charge detector (CD). When the QD is operated as a Fabry–Pérot interferometer, we find resonances with a slope in the voltage–magnetic field space and a periodicity characteristic of a Coulomb dominated effect, as already observed in previous experiments [17–19]. When the system is operated at a lower transmission where the barriers are in the tunneling regime, we observe a similar effect as in [16]. However, the amplitude modulation can be observed over a large parameter range for different filling factors, allowing the direct measurement of the charge stability diagram of capacitively and tunnel-coupled edge states. As a consequence, we can estimate the width of the incompressible region separating the edge channels inside the QD. In contrast to previous experiments, this is accomplished by using capacitances directly extracted from the measured charge stability diagram. Furthermore, we are able to investigate the CB amplitude modulation by using (time-resolved) charge detection techniques, where it

shows up as an increased/decreased tunneling rate. To our knowledge, single-electron counting has never been performed with a QD of a similar size. Direct transport measurements do not always reflect the full complexity of the edge state substructure inside a QD. In future experiments, single-electron counting might provide additional important insight into charge localization and transport in micron-sized Fabry–Pérot interferometers. Most of the proposed Fabry–Pérot interferometry experiments for probing the properties of fractional quantum Hall states assume edge states to be one-dimensional electron or composite fermion channels with negligible interaction between compressible regions. We show that when the edge states are confined to the QD, a complex behavior with compressible and incompressible regions is observed. The observed tunnel coupling between the different compressible regions, i.e. the presence of tunnel-coupled alternative paths, might influence the outcomes of the proposed interferometry experiments.

2. Experimental details

The QD has been fabricated on a Hall bar, defined by wet-etching of a single-side doped GaAs/Al$_x$Ga$_{1-x}$As heterostructure with a mobility of $8.1 \times 10^6 \, \text{cm}^2 \, \text{V} \, \text{s}^{-1}$ and an electron density of $1.15 \times 10^{11} \, \text{cm}^{-2}$. These structures employ a reduced proportion of Al in the spacer layer between the doping plane and the two-dimensional electron gas (2DEG) ($x = 0.24$ compared to the $x = 0.30$ or 0.33 which are most widely used), which was shown to favor the formation of the $\nu = \frac{5}{2}$ state [20]. The electron gas resides 320 nm below the surface. Optical lithography, combined with chemical etching and metal evaporation, are used to define the mesa, ohmic contacts and topgate leads. The QD and CD gates are defined by electron-beam lithography with subsequent metal evaporation. Applying a negative voltage of $V_G \approx -0.5 \, \text{V}$ to the topgates depletes the electron gas underneath. Compared to double-side doped quantum wells with δ-doped screening layers, this structure allows for a much better gateability [21]: the conductance of a single QPC is non-hysteretic and stable in time. Measurements have been made in a dry dilution refrigerator at a base temperature of $T_{MC} \approx 10 \, \text{mK}$ and in magnetic fields between $B = 0$ and 5 T, using standard four-terminal lock-in measurement techniques. A constant ac voltage modulation of amplitude $< 20 \, \mu\text{V}$ has been applied via a current-to-voltage converter.

3. Results and discussion

3.1. Zero magnetic field transport

Figure 1(a) shows the topgate layout of the QD that has been used for the measurements. The two 800 nm wide QPCs with a channel length of 600 nm serve as tunnel barriers of the 1.6 μm wide QD. The employed QPCs have shown to result in an almost harmonic confinement potential, apart from the regime very close to pinch-off [21]. The special geometry ensures a smooth QPC potential, which is believed to favor the self-consistent formation of separated edge states.

In addition to the plunger gate (PG) that allows for tuning of the electrochemical potential of the QD, a QPC that serves as a CD [22, 23] has been implemented. When QPC$_1$ and QPC$_2$ are in the tunneling regime, finite-bias measurements give rise to characteristic Coulomb diamonds (figure 1(b)), from which we extract charging energies of about 100 μeV. The Coulomb
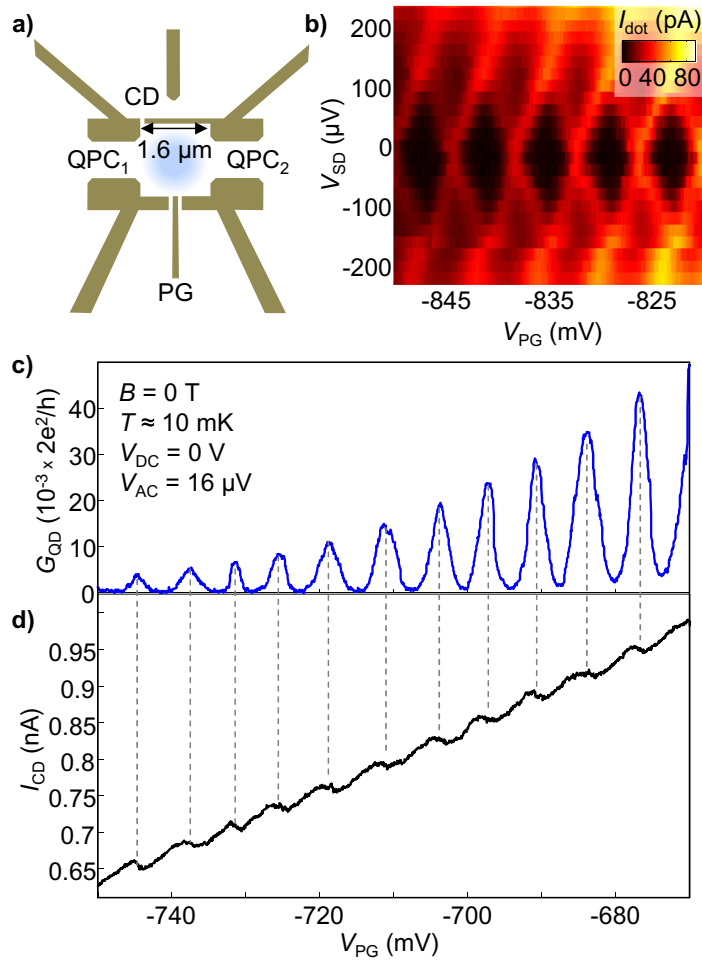
Figure 1. (a) Topgate layout of the QD. The two 800 nm wide QPCs (QPC_1 and QPC_2) were designed to provide a smooth saddle-point potential. A third, 600 nm wide QPC serves as a CD. The sample stability is sufficient for measuring regular and stable CB diamonds (b). Despite the dot's large size, single-electron charging events can be resolved in the CD (d) as well as in the direct current (c).

diamond measurement also demonstrates the good stability and control of the QD. Sharp kinks in the CD current I_{CD} (figure 1(d)), aligned with peaks in the dot conductance G_{QD}, indicate addition/depletion of a single electron from the QD. By pinching off the tunnel barriers even more, time-resolved single electron counting [23–25] is possible for rates below approximately 50 Hz.

3.2. Non-cyclic depopulation of edge channels

For a bulk filling factor of $\nu_{bulk} = 2$, a filling factor in the QD of $\nu_{QD} \approx 2$ and $\nu_{QPC} \approx 0$, we have two spin-split edge states that are formed in the bulk, as well as in the dot. They are tunnel-coupled across the QPCs (see the schematic inset of figure 2(a)) and CB oscillations are distinctly different from zero magnetic field measurements in this case: the peak height of adjacent CB peaks alternates between two different values (figure 2(a)). After five peaks of
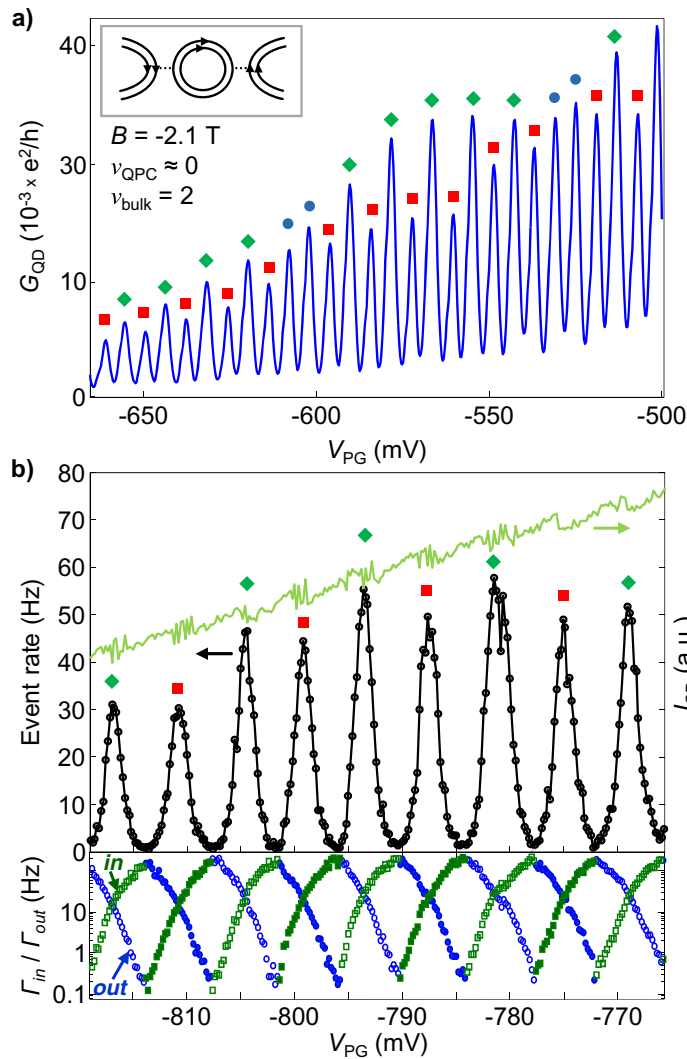
Figure 2. (a) CB peaks for a bulk filling factor of 2. When depleting the dot with the PG, Coulomb peaks with a high/low peak current (diamonds/squares) are observed, interrupted by two peaks of a similar magnitude (filled circles). The alternating pattern also shows up in the number of single electron charging events in a more pinched-off regime (b). Here, the rate of events is shown in black, with the corresponding CD current I_{CD} (shifted and scaled) in green (gray). Tunneling-in (Γ_{in}) and tunneling-out (Γ_{out}) rates for different Coulomb peaks are shown below.

high amplitude (marked by diamonds) and six peaks of low amplitude (squares), two peaks of a similar height (filled circles) appear. The alternating peak height can also be seen in the single-electron counting regime (figure 2(b)). Here, the rate of tunneling events between dot, source and drain (black line, extracted from a time-resolved measurement of the CD current) is plotted as a function of the PG voltage V_{PG}. The contrast between peaks of high and low amplitude is lower than in the direct transport measurements. However, taking into account the amplitude dependence on the PG voltage (decreased Coulomb peak height as V_{PG} is decreased), we still have a peak height difference of roughly 15%, bigger than our detection error. Tunneling-in
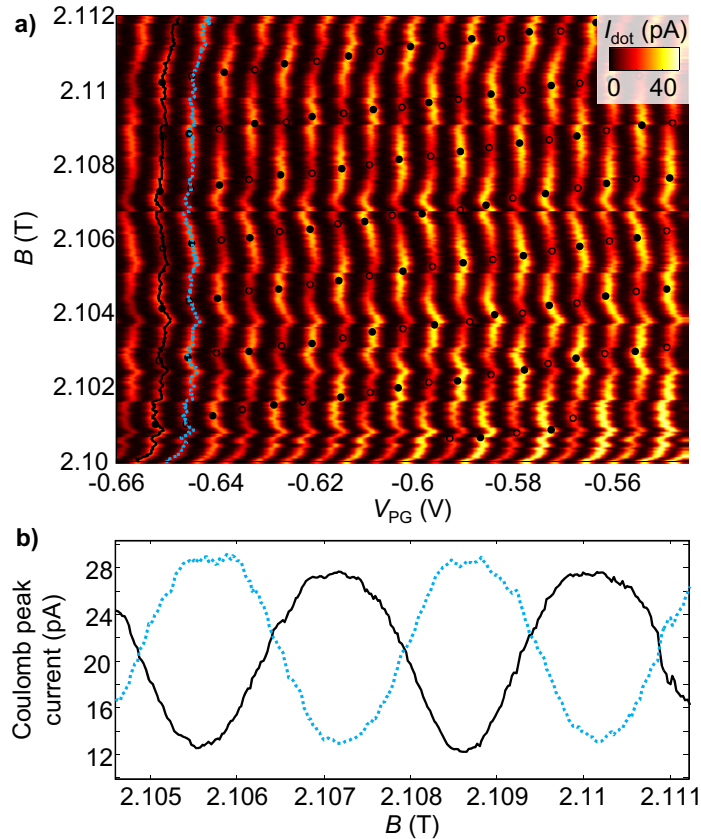
Figure 3. (a) CB peaks, measured as a function of magnetic field and voltage applied to the PG. Minima and maxima of the Coulomb peak current are extracted numerically and indicated by filled/empty circles. (b) Amplitude of two neighboring Coulomb peaks (position indicated in black/blue (gray) in (a)) as a function of the magnetic field.

(Γ_{in}) and tunneling-out (Γ_{out}) rates have been extracted from time-resolved measurements of the CD conductance. Apart from the different event rates at the Coulomb peak maxima, no further evidence of additional levels contributing to transport or more complex processes, such as electron bunching [26], could be found. As argued later, this means that tunneling processes within the dot are much faster than processes between the QD and the leads. Measuring the CB oscillations as a function of PG voltage and magnetic field, a complex pattern of peak maxima is found (figure 3(a)). By extracting the peak amplitude minima (empty circles) and maxima (filled circles) numerically, it can be seen that they are distributed according to a tilted chessboard pattern, as indicated by filled and empty circles in figure 3(a). Along a Coulomb peak (black or blue (gray) line in figures 3(a) and (b)), the peak current is modulated as a function of the magnetic field (figure 3(b)). Neighboring Coulomb peaks show opposite amplitude dependences.

Dominant shifts and drifts of the CB peaks in the measurement of figure 3(a), make it impossible to investigate the absolute position of the peaks. However, modulations in the voltage spacing ΔV_{PG} of two adjacent peaks can clearly be observed (figure 4(c)). Here, we plot ΔV_{PG} of two successive CB peaks, offset in the x-direction for better visibility. Similar measurements can be made for a bulk filling factor $\nu_{bulk} \approx 4$. In this case, bulk transport measurements suggest
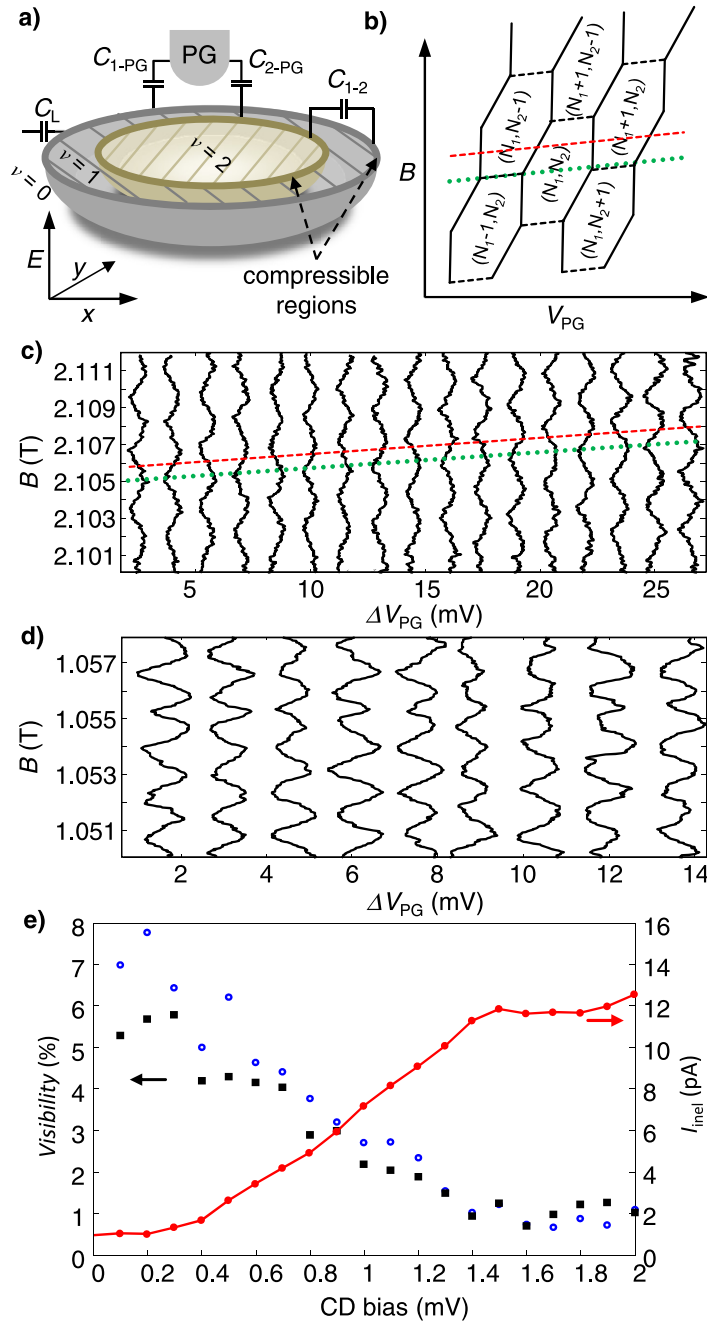
Figure 4. (a) Capacitive model for two coupled edge channels. The discoidal energy levels LL1 and LL2 are separated in energy, but overlap spatially. Tunneling of charges is possible in between the compressible regions where the LLs cross the Fermi energy. (b) Exemplary charge stability diagram for a double QD. Along the magnetic field axis, electrons are mainly redistributed in between LL1 and LL2 as well as slightly changing the total population by varying the total energy. A variation of the PG voltage V_{PG} mainly influences the total electron population of the dot. The dashed (red) line indicates a situation in which the edge channels are cyclically depopulated, giving rise to a maximal

IOP Institute of Physics ⦿ DEUTSCHE PHYSIKALISCHE GESELLSCHAFT

Figure 4. (Continued) height difference between neighboring peaks, as transport takes place alternately via LL1 or LL2. Along the dotted (green) line, neighboring Coulomb peaks lie close to the triple points and thus are thermally averaged and equally high. The PG voltage difference between successive Coulomb peaks is shown in (c) for $\nu_{QD} \approx 2$ and in (d) for $\nu_{QD} \approx 4$. The lines have been shifted closer together for better visibility. The dotted (green) line marks the position of Coulomb peaks of equal height; along the dashed (red) line, the peak height difference of neighboring peaks is maximal. (e) Visibility of two Coulomb peak pairs as a function of the CD bias ($G_{CD} \approx 0.25\frac{e^2}{h}$). Increasing the bias lowers the peak height difference visibility while it increases the inelastic current through the QD.

two spin-degenerate edge states separated by an incompressible region. Figure 4(d) shows the voltage distance between adjacent CB peaks for this case.

The described behavior can be explained by a capacitive model [16]: at a filling factor of $\nu_{QD} = 2$ in the QD, the edge states corresponding to the spin-split lowest Landau level (LL) form compressible regions inside the QD. We denote the lower/upper spin-split part of the lowest LL by LL1 and LL2. The width of these regions is dictated by self-consistency of the edge potential and the electrostatic potential contribution of the electron density [27]. In-between the compressible rings (shown schematically in figure 4(a) as thick lines), an incompressible region with a magnetic field-dependent width is formed (hatched region). In this situation, electrons in both LLs populate the whole disc-shaped area in the QD. However, only the compressible regions contribute to electron transport. Both spin-split levels inside the dot are tunnel coupled to source and drain and capacitively coupled to the PG, as well as to the leads. In addition, there is mutual capacitive coupling between the two spin-split levels. Although they overlap spatially, the electronic states are only tunnel coupled via the compressible regions of both discs. This configuration is an analogue to a double QD system, which in this case is formed by energetically separated, but spatially overlapping electronic states. Here, two main effects determine the configuration of the QD: firstly, increasing the magnetic field increases the degeneracy of the LLs. For a constant number of electrons in the dot, this corresponds to a redistribution of electrons between LL1 and LL2. In addition to that, an increased magnetic field also leads to an increased spin splitting, translating to a larger separation and therefore reduced tunnel coupling in between the compressible regions. However, for the magnetic field ranges studied here, this tunnel coupling variation can be neglected. Secondly, the total population of the QD can be tuned via the PG, which couples to both LL1 and LL2. Due to the spatial overlap and the common center of mass of LL1 and LL2, we expect that the capacitive coupling of both regions to the PG is similarly strong. The conversion factors between energy and gate voltage, the lever arms α_1 and α_2 for discs 1 and 2 thus are expected to be very similar, with a slightly bigger α_1, considering the larger contribution to the capacitive coupling at the edge closer to the PG. In this configuration, each spin-split level, LL1 and LL2, can be seen as a separate QD with single-particle energies $\frac{1}{2}\hbar\omega_c \pm \frac{1}{2}g\mu_B B$ and charging energies of $\frac{e^2}{C_1}$ and $\frac{e^2}{C_2}$, where C_1 and C_2 are the self-capacitances of discs 1 and 2. With the mutual capacitance C_{1-2}, the total energy of the double QD with N_1 electrons in LL 1 and N_2 electrons in LL 2 can be

expressed as

$$E(N_1, N_2) = \tfrac{1}{2}\hbar\omega_c(N_1 + N_2) - \tfrac{1}{2}g\mu_B B N_1 + \tfrac{1}{2}g\mu_B B N_2 - e\alpha_1 V_{PG} N_1 - e\alpha_2 V_{PG} N_2$$
$$+ \frac{e^2}{2C_1}N_1^2 + \frac{e^2}{2C_2}N_2^2 + \frac{e^2}{C_{1-2}}N_1 N_2,$$

where $\omega_c = \frac{eB}{m^*}$ is the cyclotron frequency. The charge configuration of such a double QD system can be described by a charge stability diagram with hexagonal regions of constant charge configuration (N_1, N_2) [28, 29]. From the total energy, we may find the conditions for the magnetic field and PG voltage values along the boundary lines of this diagram (constant terms have been omitted):

Transition	B–V_{PG} dependence
$(N_1, N_2) \rightarrow (N_1 + 1, N_2 - 1)$	$B \propto \dfrac{e}{g\mu_B} \underbrace{(\alpha_2 - \alpha_1)}_{\approx 0} V_{PG}$
$(N_1, N_2) \rightarrow (N_1 + 1, N_2)$	$B \propto \dfrac{2e}{\frac{\hbar e}{m^*} - g\mu_B} \underbrace{\alpha_1}_{>0} V_{PG}$
$(N_1, N_2) \rightarrow (N_1, N_2 + 1)$	$B \propto \dfrac{2e}{\frac{\hbar e}{m^*} + g\mu_B} \underbrace{\alpha_2}_{>0} V_{PG}$

In figure 4(b), such a charge stability diagram is shown schematically for given electron numbers in LL 1 and 2, (N_1, N_2), as a function of the magnetic field B and the PG voltage V_{PG}. Due to the comparable size of the capacitances C_1, C_2 and C_{1-2}, the hexagons have a nearly rectangular shape (from the measured charge stability diagrams explained later, it can be extracted that $C_{1-2} \approx 0.87 \times C_1$). Coulomb peaks occur whenever charge configurations of N_i and $N_i + 1$ electrons on LL1 ($i = 1$) or LL2 ($i = 2$) are energetically degenerate. A high CB peak current is observed if the electrochemical potential of LL1 is aligned with the Fermi energy in source and drain, and a low peak current corresponds to the alignment of the electrochemical potential of LL2 with the Fermi energy. The reason for this peak height modulation is the different lateral tunneling distances. The dashed (red) line in figure 4(b) indicates a V_{PG} trace, in which the amplitude difference between adjacent peaks is maximal (alternating transport via LL1 or LL2). Along this line, the charge degeneracy lines are crossed at a maximum distance from the triple points. In contrast, the dotted (green) line corresponds to a case where charge configurations that contribute to high and low amplitude are energetically close. Traversing the boundaries of the charge stability diagram near a triple point leads to thermal averaging of these two configurations, resulting in peaks of approximately equal height (as marked by filled circles in figure 2(a)). Due to the slightly tilted hexagons, the high–low pattern is found again by further varying V_{PG}. In addition, slightly different charging energies of the two LLs lead to a distorted hexagon pattern.

A change of magnetic field has two effects: for a situation with a constant total number of charges, the addition of flux quanta to the interior of the QD increases the degeneracy of both LL and their splitting, thus redistributing electrons between LL1 and LL2. A change of the magnetic field also influences the total population of the dot, as it shifts QD energy levels

IOP Institute of Physics ⟐ DEUTSCHE PHYSIKALISCHE GESELLSCHAFT

relative to the Fermi energy in the leads. The (red) dashed line in figure 4(c) corresponds to the position of CB peaks with maximally modulated amplitudes. In agreement with the model illustrated in figure 4(b), these lines correspond to approximately equal separation of adjacent peaks. For the second case, where the amplitude difference is thermally averaged (dotted (green) line in figure 4(b)), we expect and observe in figure 4(c) (along the green dotted line) alternating high and low ΔV_{PG}.

To identify whether the amplitude modulation is caused by only different lateral tunneling distances or an activated tunneling process, we can look at figure 4(e): here we measure the relative visibility $((G_{LL1} - G_{LL2})/(G_{LL1}/2 + G_{LL2}/2))$ of two thermally broadened pairs of Coulomb peaks, as a function of the bias that has been applied to the CD QPC at its maximum sensitivity (in our case $G \approx 0.25\frac{e^2}{h}$ due to a localization in the QPC). The amplitude difference is observed to vanish when the bias is increased. The CD back-action is expected to increase the broadening of the Fermi–Dirac distribution of the leads. We are in the multilevel transport regime ($h\Gamma \ll \Delta E \lesssim k_B T$, but not $\Delta E \ll k_B T$).[2]

The tunneling rate to both regions increases, as additional levels lie within the broadening of the Fermi–Dirac distribution. The broadening also leads to an increased occupation of the excited states of LL1 compared to the ground state of LL2 and thus an increased activated tunneling rate to LL2, which could explain why the amplitude difference vanishes. From the 40% maximum amplitude modulation between neighboring peaks, we can extract an energy-level separation of $\Delta E \approx 3\,\mu$eV, using $\exp(-\Delta E/k_B T) \approx 0.6$ and assuming a typical electron temperature of 60 mK. This is the order of magnitude expected for a dot of the given size.

One may ask whether there is any direct evidence that the second compressible region LL2 is involved in transport. In the situation where the electrochemical potential of LL2 is aligned with the potential of the leads (with a tunneling rate between LL1 and LL2 which is much slower than the tunneling rate between the leads and LL1), there are two sequential processes involved in an electron transfer from the leads to the QD: firstly, the fast activated tunneling of an electron to LL1 and back to the leads; secondly, slow tunneling from LL1 to LL2. Due to the very similar capacitive coupling of LL1 and LL2 to the CD, we are not able to resolve charge redistributions between those regions. From LL2, the electron can only escape with activated tunneling through LL1. While the electron has not left LL2, LL1 is blocked for further electron tunneling, due to the strong capacitive coupling C_{1-2}. The two tunneling processes would lead to electron bunching in the CD signal. However, such a bunching is not observed in the experiment, suggesting that the interdot tunneling rate is very high (compared to the tunneling rate between QD and the leads) in our case.

Using the extracted interdot capacitance $C_{1-2} \approx 0.87C_1$, we can make a rough statement about the spatial extent of the QD wave function. Modeling the interdot capacitance as a simple plate capacitor with a capacitance proportional to the plate area, we expect the area of LL2 to be roughly 87% of the area of LL1. The area of LL1 can be estimated from the lithographic size and the gate depletion lengths of the QD, yielding $A \approx 0.64\,\mu$m^2. For rectangular QDs, this results in a difference of the side lengths of 54 nm. When the finite width of the edge states is neglected, this corresponds to a width of 27 nm of the incompressible region. Numerical calculations of bulk samples have predicted a width of approximately 20 nm for the incompressible region,

---

[2] In this regime, the Coulomb peak conductance is expected to have a small temperature dependence [30, 31], until either $k_B T \ll \Delta E$ or $k_B T \approx e^2/C$. (Note, however, that this does not hold whenever $h\Gamma \approx \Delta E$, where the amplitudes may have an irregular and even nonmonotonic dependence on temperature [32].)

corresponding to a local filling factor of 2 [33]. The enhanced value for our case could be the result of the simplicity of the model used, which just allows for an order of magnitude estimate, or a smoother confinement potential and increased electron–electron interaction due to confinement. Similarly, a width of approximately 50 nm can be extracted from $C_{1-2} \approx 0.77 C_1$ in the case of $\nu_{QD} \approx 4$. The increased width in this case is expected, as LL1 and LL2 are split by the larger cyclotron energy.

4. Conclusion

In summary, we have investigated transport through a large QD, fabricated on a high-mobility wafer. Single-electron counting techniques, as well as direct current transport, have been used to understand better the inner structure of the QD for different filling factors. The periodic modulation of the conductance peak amplitude and spacing can be explained by a capacitive model involving compressible and incompressible regions inside the dot. The high tunability of the device allowed investigation of the transport in the tunneling regime, as well as in a regime with edge states perfectly transmitted through the dot (see the appendix). In this case, conductance oscillations governed by a CB mechanism have been observed.

Acknowledgments

Appendix. Transport in the Fabry–Pérot regime

The Hall voltage drop across the QD (V_{diag}, see the inset of figure A.1(a)) gives access to the conductance through both constrictions [17]. When both QPCs are tuned to the same transmission ($G \approx 10 \frac{e^2}{h}$ at $B = 0$) by applying a negative topgate voltage and the magnetic field is varied, we find the conductances through the constrictions quantized in multiples of $\frac{e^2}{h}$ (figure A.1(a)). In this configuration, edge states are formed in the bulk, in the QD and in the QPCs. In the QPCs, the filling factor is lower than in bulk and QD: $\nu_{QPC} < \nu_{QD}, \nu_{\text{bulk}}$ (for our large dot $\nu_{QD} \approx \nu_{\text{bulk}}$). We note that ν_{QPC} edge states pass the QD and contribute to the diagonal conductance, while ($\nu_{QD} - \nu_{QPC}$) edge states are confined inside the QD. On the riser of the conductance-plateaus (i.e. the low magnetic field side), periodic conductance oscillations are observed (figure A.1(b) for $\nu_{QPC} \approx 2$, figure A.1(c) for $\nu_{QPC} \approx 1$). The peaks of these oscillations are shifted to lower magnetic fields when the PG voltage is decreased (figures A.1(b) and (c)). The strength of this shift depends on the filling factor inside the QPCs ($\Delta B \approx 1.0$ mT for $\nu_{QPC} \approx 2$, $\Delta B \approx 1.9$ mT for $\nu_{QPC} \approx 1$, a smooth background has been subtracted). However, the PG spacing ΔV_{PG} is similar for both cases ($\Delta V_{PG} \approx 7.2$ mV for $\nu_{QPC} \approx 2$, $\Delta V_{PG} \approx 7.9$ mV for $\nu_{QPC} \approx 1$). This scaling with the QPC filling factor, as well as the direction of the shift, are both contrary to what is expected for an Aharonov–Bohm interferometer [34]. Instead, the results are consistent with previous experiments and show that transport is governed by a CB mechanism [17–19]. In this picture, the slope of the magnetoconductance oscillations is caused by the capacitive coupling of confined and transmitted edge states in the QD instead of a direct
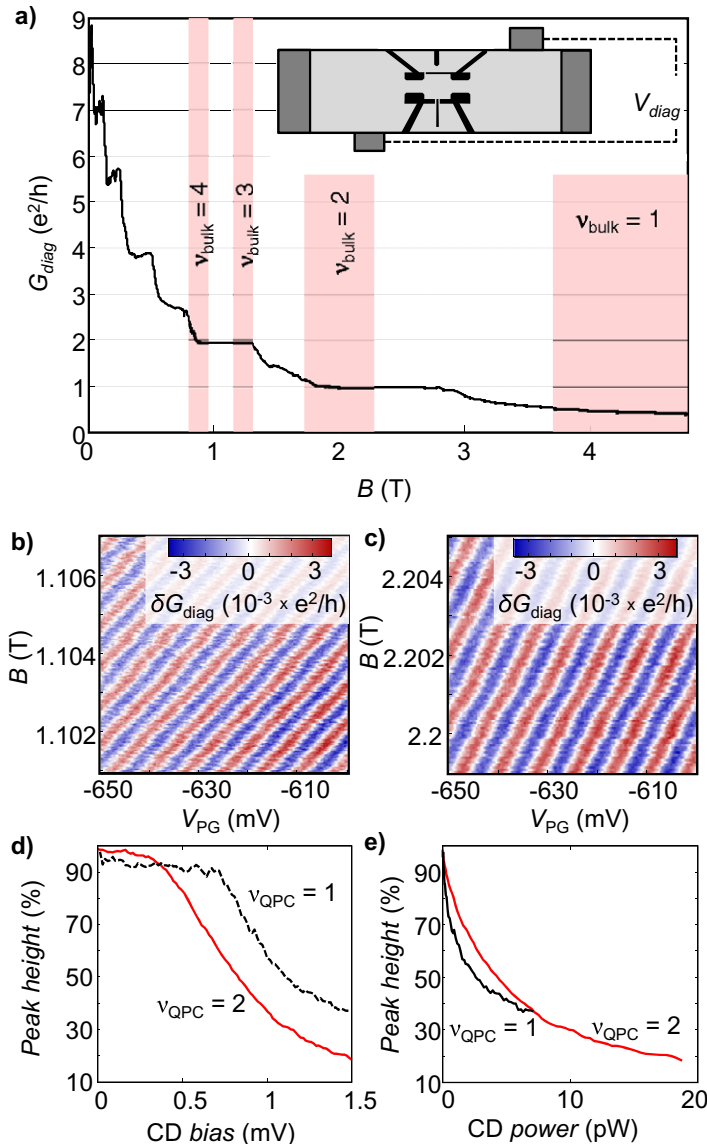
Figure A.1. (a) From the Hall voltage drop V_{diag} diagonally across the QD (inset), the effective conductance through the QD can be extracted. Here, we show G_{diag} for a fixed voltage applied to the topgates, as a function of magnetic field. G_{diag} is quantized in multiples of $\frac{e^2}{h}$. Shaded regions indicate the filling factor ν_{bulk} of the bulk at the corresponding magnetic field values. On the riser of the conductance plateaus, magnetoresistance oscillations are observed. Their dependence on magnetic field and PG voltages is shown in (b) for $\nu_{QPC} \approx 2$, $\nu_{bulk} \approx 4$ and in (c) for $\nu_{QPC} \approx 1$, $\nu_{bulk} \approx 2$. Increasing the bias and the power applied to the CD QPC, respectively, greatly reduces the peak height of the observed magnetoresistance oscillations (d), (e).

effect of the PG on the interferometer area as in the Aharonov–Bohm case. Increasing the bias applied to the CD QPC ($G \approx 0.2\frac{e^2}{h}$, figure A.1(d)) decreases the amplitude of the oscillations, while the background of the conductance approaches its plateau value.

References

[1] Stormer H L, Chang A, Tsui D C, Hwang J C M, Gossard A C and Wiegmann W 1983 *Phys. Rev. Lett.* **50** 1953–6

[2] Tsui D C, Stormer H L and Gossard A C 1982 *Phys. Rev. Lett.* **48** 1559–62

[3] Laughlin R B 1983 *Phys. Rev. Lett.* **50** 1395–8

[4] Willett R, Eisenstein J P, Störmer H L, Tsui D C, Gossard A C and English J H 1987 *Phys. Rev. Lett.* **59** 1776–9

[5] Moore G and Read N 1991 *Nucl. Phys.* B **360** 362–96

[6] Read N and Rezayi E 1999 *Phys. Rev.* B **59** 8084–92

[7] Nayak C, Simon S H, Stern A, Freedman M and Das Sarma S 2008 *Rev. Mod. Phys.* **80** 1083–159

[8] Stern A and Halperin B I 2006 *Phys. Rev. Lett.* **96** 016802

[9] Bonderson P, Kitaev A and Shtengel K 2006 *Phys. Rev. Lett.* **96** 016803

[10] Das Sarma S, Freedman M and Nayak C 2005 *Phys. Rev. Lett.* **94** 166802

[11] Ilan R, Grosfeld E and Stern A 2008 *Phys. Rev. Lett.* **100** 086803

[12] Bonderson P, Shtengel K and Slingerland J K 2006 *Phys. Rev. Lett.* **97** 016401

[13] Rogge M C, Fühner C and Haug R J 2006 *Phys. Rev. Lett.* **97** 176801

[14] Ciorga M, Sachrajda A S, Hawrylak P, Gould C, Zawadzki P, Jullian S, Feng Y and Wasilewski Z 2000 *Phys. Rev.* B **61** R16315–8

[15] Staring A A M, Alphenaar B W, van Houten H, Molenkamp L W, Buyk O J A, Mabesoone M A A and Foxon C T 1992 *Phys. Rev.* B **46** 12869–72

[16] Heinzel T, Wharam D A, Kotthaus J P, Böhm G, Klein W, Tränkle G and Weimann G 1994 *Phys. Rev.* B **50** 15113

[17] Zhang Y, McClure D T, Levenson-Falk E M, Marcus C M, Pfeiffer L N and West K W 2009 *Phys. Rev.* B **79** 241304

[18] Camino F E, Zhou W and Goldman V J 2007 *Phys. Rev.* B **76** 155305

[19] Ofek N, Bid A, Heiblum M, Stern A, Umansky V and Mahalu D 2010 *Proc. Natl Acad. Sci. USA* **107** 5276–81

[20] Gamez G and Muraki K 2011 arXiv:1101.5856

[21] Rössler C, Baer S, de Wiljes E, Ardelt P L, Ihn T, Ensslin K, Reichl C and Wegscheider W 2011 *New J. Phys.* **13** 113006

[22] Field M, Smith C G, Pepper M, Ritchie D A, Frost J E F, Jones G A C and Hasko D G 1993 *Phys. Rev. Lett.* **70** 1311–4

[23] Ihn T, Gustavsson S, Gasser U, Küng B, Müller T, Schleser R, Sigrist M, Shorubalko I, Leturcq R and Ensslin K 2009 *Solid State Commun.* **149** 1419–26

[24] Elzerman J M, Hanson R, Willems van Beveren L H, Witkamp B, Vandersypen L M K and Kouwenhoven L P 2004 *Nature* **430** 431–5

[25] Schleser R, Ruh E, Ihn T, Ensslin K, Driscoll D C and Gossard A C 2004 *Appl. Phys. Lett.* **85** 2005

[26] Gustavsson S, Leturcq R, Simovič B, Schleser R, Studerus P, Ihn T, Ensslin K, Driscoll D C and Gossard A C 2006 *Phys. Rev.* B **74** 195305

[27] Chklovskii D B, Shklovskii B I and Glazman L I 1992 *Phys. Rev.* B **46** 4026–34

[28] Pothier H, Lafarge P, Urbina C, Esteve D and Devoret M H 1992 *Europhys. Lett.* **17** 249–54

[29] Ruzin I M, Chandrasekhar V, Levin E I and Glazman L I 1992 *Phys. Rev.* B **45** 13469–78

[30] Beenakker C W J 1991 *Phys. Rev.* B **44** 1646–56

[31] Kouwenhoven L P, Marcus C M, McEuen P, Tarucha S, Westervelt R and Wingreen N 1997 Electron transport in quantum dots *Mesoscopic Electron Transport* (*Proc. NATO Advanced Study Institute on Mesoscopic Electron Transport) (Curaçao, Netherland Antilles, 25 June–5 July 1996*) (Dordrecht: Kluwer Academic)

[32] Meir Y, Wingreen N S and Lee P A 1991 *Phys. Rev. Lett.* **66** 3048–51

[33] Lier K and Gerhardts R R 1994 *Phys. Rev.* B **50** 7757–67

[34] Halperin B I, Stern A, Neder I and Rosenow B 2011 *Phys. Rev.* B **83** 155440